Proceedings of ICFD13:
Thirteenth International Conference of Fluid Dynamics
21-22 December, 2018, Cairo, EGYPT

ICFD13-EG-6095

Role of impinging jets in the biomechanical correction of the intraocular pressure (IOP) measurement

Osama Maklad *, [1], Vassilis Theofilis [1], Ahmed Elsheikh [1, 2]
[1] School of Engineering, University of Liverpool, Liverpool, UK
[2] NIHR Biomedical Research Centre for Ophthalmology, Moorfields Eye Hospital NHS Foundation Trust and UCL Institute of Ophthalmology, London, UK

ABSTRACT

Glaucoma is one of the ocular diseases which develops when the eye internal fluid cannot drain properly and intraocular pressure builds up. This can result in damage to the optic nerve and the nerve fibers from the retina and early diagnosis is very important as any damage to the eyes cannot be reversed [1]–[3]. Non-contact IOP measurement techniques like corneal response analyzers including CorVis-ST are very popular. The technique depends on impingement of an air puff to the cornea and recording the corneal response to the impact force from the puff using high speed Scheimpflug imaging. The aim of this study is to improve the accuracy of the IOP measurements by considering the fluid structure interaction effect between the cornea, the air puff and the eye internal fluid through a parametric study of numerical models and their comparisons with the clinical data.

KEYWORDS:

Impinging jets; Aero elasticity; Non-Contact Tonometry; Ocular biomechanics; Glaucoma, Intraocular Pressure (IOP); Computational Fluid Dynamics (CFD); Finite Element Analysis (FEA); Fluid Structure Interaction (FSI).

1. INTRODUCTION

The basic theory of the CFD impinging air puff is the round jet diffusion and impingement theory. The impinging jets have different variety of important applications such as cooling and drying, they are also representative models for the jets in vertical take-off and landing aircrafts and rockets or in the simulation of the atmospheric microbursts. The flow characteristics of impinging jets depend on different parameters, such as jet orifice diameter, nozzle to impingement surface distance, jet confinement, radial distance from stagnation point, angle of impingement, surface curvature & roughness, nozzle exit geometry and turbulence intensity[4]–[6]. By studying the air puff and its flow characteristics, it has been found that it's a turbulent jet with maximum Reynolds number (23702.26) which means that it's required to simulate highly disturbed flow with highly deformable boundaries. The jet split into 3 regions; the "free" jet region, the impingement or stagnation region, and the wall-jet region.

The round jet is characterized by the continuous increase of the boundary shear layer thickness. This boundary shear layer has two corresponding factors, the decrease of the jet core cross section and the increase of the jet diameter as shown in Figure 1(a). The core length depends on the inner angle of diffusion, about 4-5^{o} and around 8^{o} for highly turbulent impinging jets [7]. Figure 1(b) shows three observed regions from an impinging jet: the "free" jet region, the impingement or stagnation region, and the wall-jet region. Beltaos et al. [7] have studied the free and impinging jet phenomena and provided a detailed experimental and analytical study of plane turbulent impinging jets.

1.1 Free jet region

From the name "free", this indicates the remote part of the jet from the wall in which the turbulence is due to the mean velocity fluctuations and the surrounding fluid is entrained or swept along the jet with a flat-topped velocity profile.

(a)

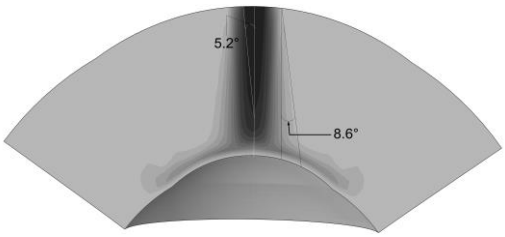

(b)

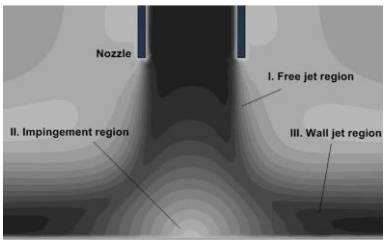

Fig. 1 Round impinging jet diffusion (a), the impinging jet different regions (b)

Miller et al.[8], [9] have studied the static pressure distribution and turbulence properties in the free turbulent jets. The flow in this region is axisymmetric and depends on the dimensionless number "Reynolds number" which is characterized by three parameters the jet velocity U_j, the jet orifice diameter D and the kinematic viscosity of the fluid ν.

$$R_e = \frac{U_j . D}{\nu} \qquad (1)$$

Moreover, the velocity decay constant and the jet spread rate are not dependent on the value of Reynolds number [10]. As the distance go further from the jet orifice, the axial velocity (U_x) decreases and the half width ($r_{1/2}$) increases according to the following equations [10], [11]

$$\frac{U_x}{U_j} = \frac{B}{(X - X_0)/D} \qquad (2)$$

where B is the velocity decay constant and the jet spreads linearly with spread rate of:

$$S = \frac{dr_{\frac{1}{2}}(x)}{dx} \qquad (3)$$

1.2 Impingement jet region

As the jet approaches the impingement surface, it experiences a velocity decay in a rate depends on the initial jet profile due to the adverse pressure gradient. In the impingement jet region, closer to the surface, the streamlines will diverge away from the jet centerline. The jet fluid accelerates again when it starts moving away in the transverse direction to form a radial wall jet [12], [13].

1.3 Wall jet region

In the wall jet region, which is the direct vicinity of the impingement surface, there are strong shear stresses and velocity fluctuations greater than any normal boundary layer and a recirculation zone above the wall jet region may be observed as well [6].

1.4 Classification of Fluid Structure Interaction Problems

In fluid mechanics, solids are considered as boundary conditions only and not in terms of what they are made of. For instance, in a flow around a cylinder, the cylinder deviates the uniform flow, and prevents the fluid from penetrating the body of the cylinder. On the other hand, in solid mechanics, we solve for deformations of the solid under loading. Some of these loadings can be due to the presence of a fluid such as a deformation of a submarine under external pressure or inflation of a balloon under internal pressure or a building or a bridge subject to the wind. Usually the fluid is considered a cause of a loading at the boundary.

The two approaches can work separately in many applications with acceptable results, but in other applications, separate solutions are not accurate enough and consideration of fluid-structure interaction becomes necessary. These interactions mostly driven by practical and industrial applications such as biomechanics, aerospace, nuclear and civil engineering. Figure 2 explains the broad range of the reduced velocity and the influence of this dimensionless number on the classification of the problem and the method of solution. The most general case, which requires full coupling between the two models, is when the reduced velocity is in order of magnitude around the displacement number which is the case in the air puff test. The reduced velocity of the air puff test ranges between 0 and 10 at the maximum velocity. The displacement number of the eye model is in order of magnitude of 10^{-2}. So any approximation or selection to another method, rather than the full coupling between the two models, will have a major impact on the accuracy of the solution.

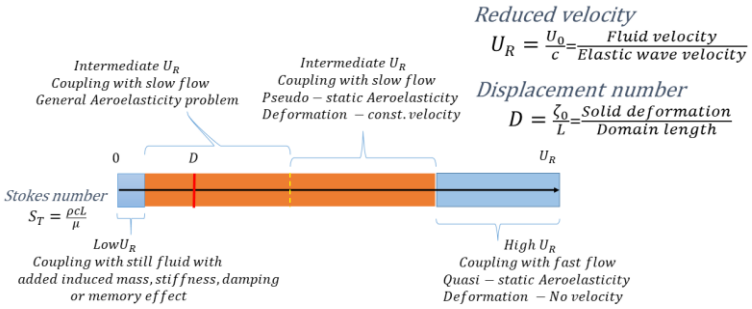

Fig. 2 classification of fluid structure interaction problems based on the value of the reduced velocity U_R

2. NUMERICAL SIMULATION METHODOLOGY

The three main parts of the air puff test simulation are the eye model, the CFD model of the air jet and the FSI coupling between them. The process starts by modelling the CFD model of the air jet first and making sure that it's working separately without any coupling or interfaces and considering the cornea as no-slip wall boundary condition. This work was followed by analysis of full eye models where the eye model has two steps; one for applying the intraocular pressure and the second for applying external air pressure. The cornea and anterior sclera were treated as a co-simulation region with interaction

boundary conditions and this was followed by generating the air domain in front of the cornea. A MATLAB code was developed to project the cornea's nodes into different layers between the cornea and the tonometer nozzle. The finite element model of the eye is coupled with the CFD turbulent model of the air puff exchanging the characteristic variables between them at every time step of the job as shown in figure 3. The structure model calculates the deformations (line 1) and sends them to the fluid model (line 2) which in turn calculates the pressure loads(line 3) and returns them back to the structure model (line 4).

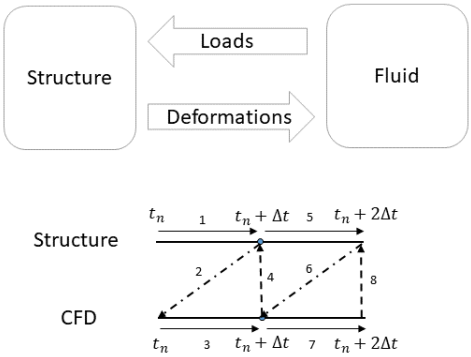

Fig. 3 Components of fluid structure interaction (FSI) analysis and flow of the solution at each time step.

2.1 Governing equations

The governing equations for the CFD model are the continuity and momentum equations. On the other hand the solid deformations are governed by the oscillator equation which includes mass, stiffness and force matrices. To create coupling between the two models, two conditions have to be satisfied at the interface; the kinematic condition and the dynamic condition. The kinematic condition is satisfied by equating the velocities of the two models at the interface which means no sliding and no mixing between the two materials, while the dynamic condition is satisfied by equating the forces at the interface, including the pressure and the viscous shear forces from the fluid model to be transferred to the force matrix of the structure model.

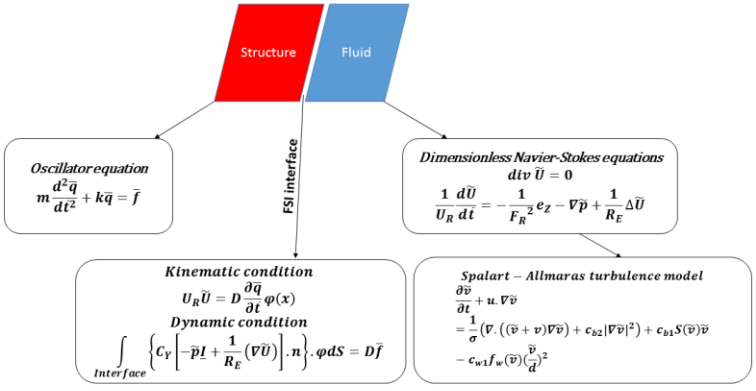

Fig. 4 Coupled dimensionless governing equations.

Figure 4 explains the dimensionless governing equations for both models and at the interface. The reduced velocity, displacement number, Cauchy number, Froude number and Reynolds number appear in the dimensionless equations.

2.2 Arbitrary Lagrangian-Eulerian (ALE) deforming-mesh

In FSI applications, where there is large solid deformations, the adaptive mesh is important for the stability of the solution and to prevent distortion of the fluid mesh. That's been done using ALE deforming mesh method which has some characteristics; the mesh motion is constrained only at the free boundaries and everywhere else the material and mesh motion are independent. The adaptive meshing incorporate two main tasks; creating a new mesh and remapping the solution variables, through a process named advection, from the old mesh to the new mesh. The meshing is created at a pre-specified frequency accompanied by a combination of mesh smoothing methods. Then, remapping the solution variables to the new mesh is second order accuracy, consistent and conserves mass and momentum. Moreover, for FSI stabilization, solution control parameters are used to maintain mesh quality and control the mesh motion. Figure 5 shows the adaptive deformable mesh of the air puff model.

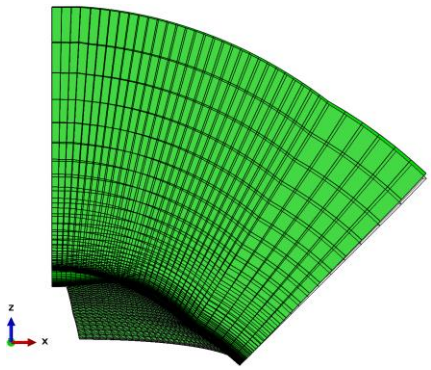

Fig. 5 ALE adaptive mesh of quarter of the air puff model.

2.3 Initial and boundary conditions

The numerical model of the air puff test is constructed in the context of a coupled computational fluid dynamics (CFD) and finite element analysis (FEA), as implemented in the software package ABAQUS (v. 6.14.2). The finite element model of the eye is prevented to move in Z-direction (Anterior-Posterior) at the equatorial nodes and the posterior and anterior pole nodes are restricted to move in X and Y directions and free to move in Z-direction. Before analysis, the stress free geometry of the eye, under zero internal pressure, were obtained [14]. The eye was the inflated with the value of IOP before applying the

external air puff pressure on the cornea from the CFD model. The material properties distribution for the cornea and sclera are reported in earlier studies [15]–[17].

For the co-simulation step to run successfully, the interaction surface in the eye and the air model should be exactly the same with the same node numbers. The eye model imports the Concentrated Force (CF) and the Lumped Mass from the CFD model and exports the deformations (U) and the velocities (V) back to the CFD model. The air jet model domain is created, using MATLAB, over the cornea and a 4 mm ring of the sclera by projecting the coordinates of the surface nodes over a distance of 11 mm from the cornea apex as shown in figure 6. The material properties of the air are defined in terms of density and viscosity. The amplitude of the air jet velocity, and its variation with time are defined according to figure 7 based on experimental data obtained from the manufacturers of Corvis-ST (Corneal Visualization Scheimpflug Technology) [16]. The CFD solution parameters are then specified in terms of momentum, pressure and transport equation solvers and which turbulence model is to be used to resolve the turbulent eddies.

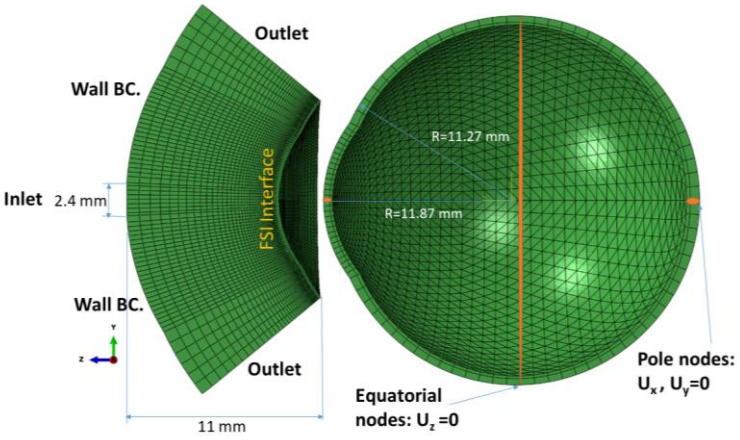

Fig. 6 Boundary conditions of the Air puff test.

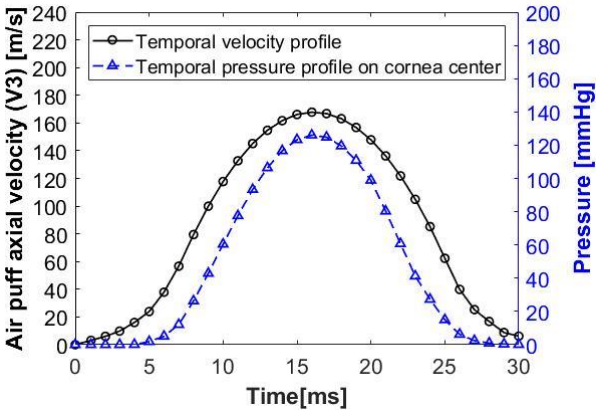

Fig. 7 Temporal velocity and pressure profiles of the air puff.

In the CFD model, the air jet inlet diameter is set to 2.4 mm and the air maximum velocity at the inlet is set to 167.8 m/s. The surface that surrounds the jet diameter is set as a wall and the side is open to the air with pressure equal to zero. Lastly, the cornea and 3 rings from the sclera are set as co-simulation interface and data exchange (FSI) surface.

3. RESULTS

3.1 CFD code validation

To validate the CFD code available in Abaqus, an impinging air jet on a fixed wall of bulk velocity of 9.6 m/s for Tummers experiment [18] and the numerically reproduced flow field on Abaqus CFD using Spallart Allmaras turbulence model are shown in figure 8. It shows good agreement with the flow field of the Laser Doppler Anemometer (LDA) experimental mean flow field. The mean axial and radial velocities at different axial traverses normal to the impingement surface are previously published in [19].

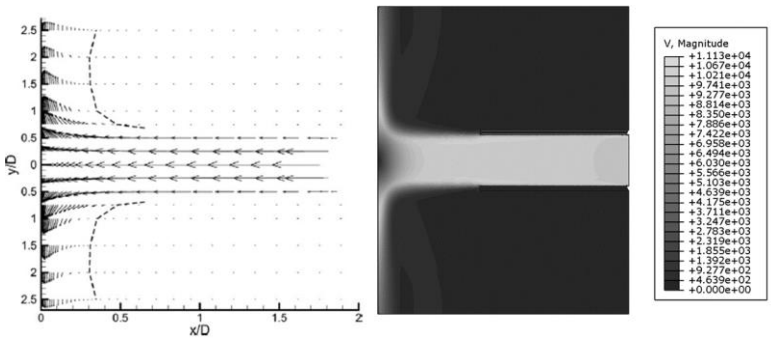

Fig. 8 CFD simulation of impinging jet on a fixed wall and LDA velocity field of Tummers experiment [16].

3.2 Air puff traverses

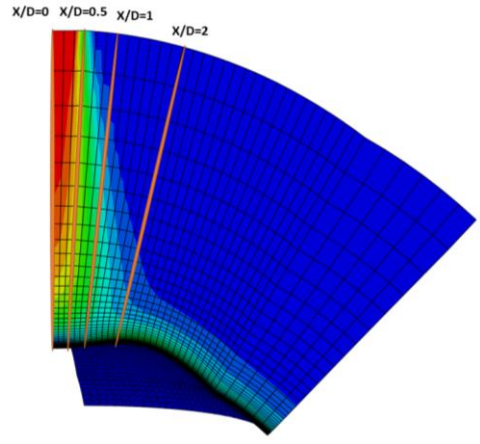

Fig. 9 Air puff normal traverses

The air puff has been analyzed to see the change of the velocity, pressure and mesh deformation during the test. Figure 10 shows the axial velocity (V3) normal to the cornea at three normal traverses (X/D=0, X/D=0.5, X/D=1) as in figure 9 and at 4 time steps.

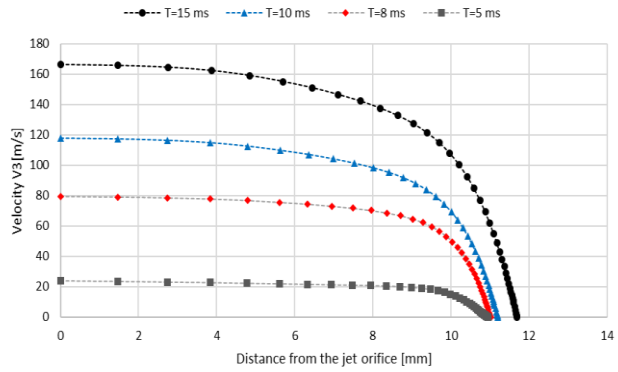

(a)

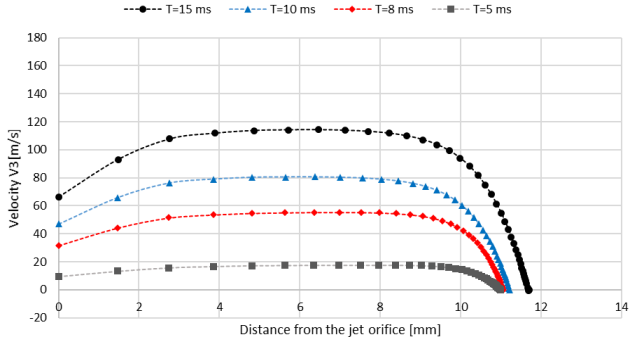

(b)

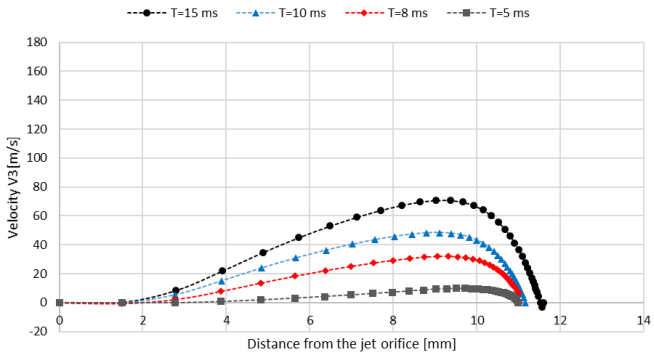

(c)

Fig. 10 Air puff normal velocity traverses (V3), At X/D=0 (a), X/D=0.5 (b), X/D=1 (c).

The pressure has been found to change with the cornea deformation and time steps. Figure 11 shows the pressure at three axial traverses (X/D=0, X/D=1, X/D=2) and 4 time steps. It's noticed from the plots that the distance from the jet at the end of every curve is increasing because of the deformation of the cornea with the time of the test.

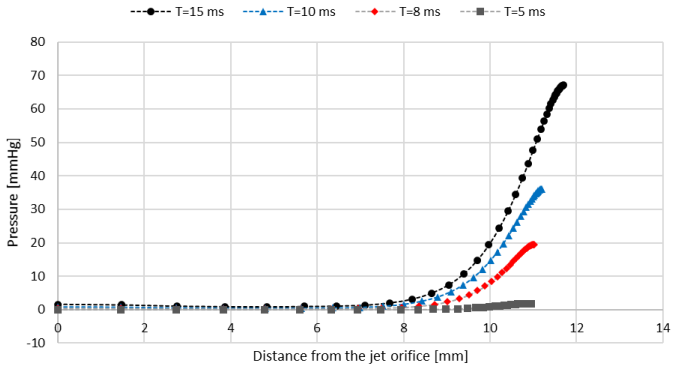

(a)

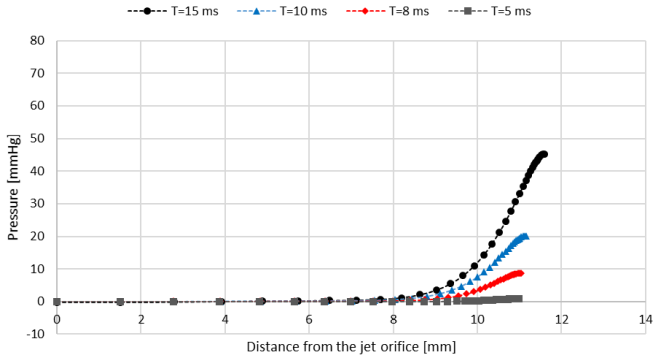

(b)

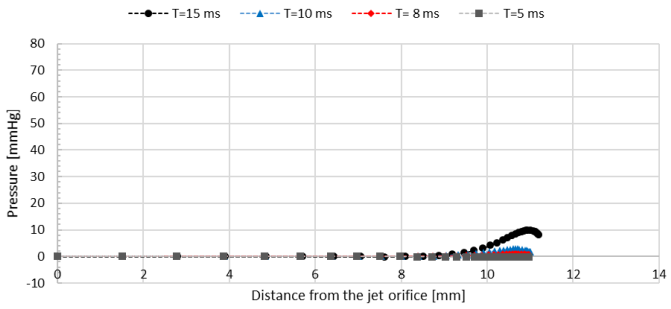

(c)

Fig. 11 Air puff pressure (P), At X/D=0 (a), X/D=1 (b), X/D=2 (c).

3.3 Pressure and deformation profiles

Fluid structure interaction has been found to have an effect on the pressure distribution on the cornea during the time of the air puff test. Figure 12 shows the pressure distribution on the cornea at different time steps during the test. Graph (a) shows the pressure distribution and the region where there is negative pressure. Graph (b) shows the progression of the cornea deformation with time and Graph (c) indicates the effect of considering the FSI effect on deformable and non-deformable cornea.

(a)

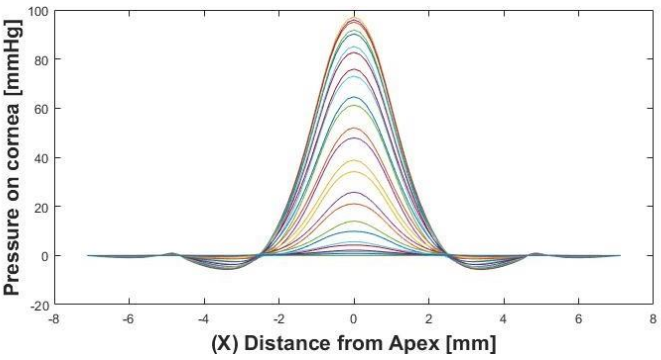

(b)

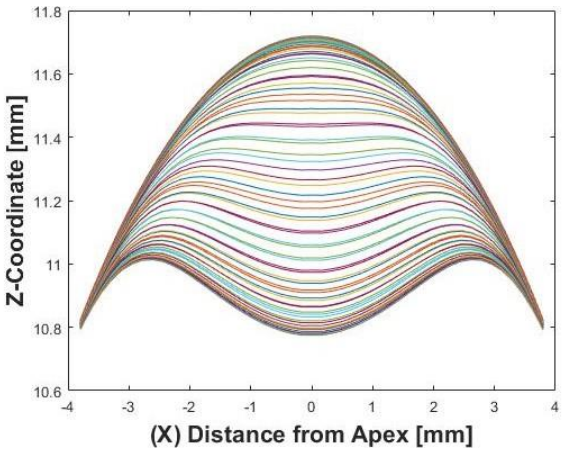

(c)

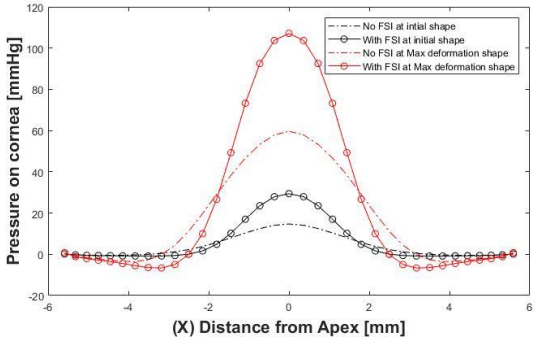

Fig. 12 Spatial pressure distribution (a), spatial corneal deformations (b), FSI effect on the pressure distribution (c).

4. DISCUSSION

The air puff test is a non-contact method to measure the eye internal pressure noninvasively, but compared to the gold standard of IOP contact measurement techniques, it's been found influenced by the biomechanical properties of the eye, either the geometry parameters like cornea thickness or radius, or the material properties which has been reported to change from person to another and with age variation as well [20]. After validating the CFD code, a parametric study has been made on 181 models with IOP range (10-15-20-25 mmHg), CCT (445-545-495-595-645 μm), R (7.4-7.8-8.4 mm) and different material properties representing the age effect. The outcome of this parametric study is producing a correction algorithm to compensate the biomechanical effect of the corneal parameters on the IOP measurement from patient to patient.

5. CONCLUSION AND FUTURE WORK

The complete coupling between the model of the eye and the air model has been accomplished. The main finding is that the pressure distribution of the air puff is changing with the time of the test and the fluid structure interaction affects the cornea deformation during the loading of the air puff depending on the stiffness properties of the cornea. A parametric study has been done to see the effect of the corneal biomechanical parameters on the IOP measurements and come up with a biomechanically corrected equation. The next required work is to compare these numerical results with more experimental data from human and porcine eyes.

NOMENCLATURE

IOP	Intraocular Pressure
CFD	Computational Fluid Dynamics
FEA	Finite Element Analysis
FSI	Fluid Structure Interaction
CF	Concentrated Force
LDA	Laser Doppler Anemometer
ALE	Arbitrary Lagrangian-Eulerian
U_R	Reduced Velocity
U_j	Jet Velocity

ACKNOWLEDGMENTS

I would like to acknowledge Prof. Ahmed Elsheikh and the Biomechanical Engineering Group (BIOEG) at the University of Liverpool for the support during my time in the PhD. Also, would like to thank Prof. Vassilis Theofilis for his constructive feedback and generous support during all the stages of this study.

REFERENCES

[1] H. A. Quigley, "Glaucoma.," *Lancet (London, England)*, vol. 377, no. 9774, pp. 1367–77, 2011.

[2] I. G. Management, "The Role of Ocular Biomechanics," *Rev. Optom.*, vol. October, pp. 49–52, 2008.

[3] E. M., A. Elsheikh, and P. Gunvant, "Tonometry – Past, Present and Future," *Glaucoma - Curr. Clin. Res. Asp.*, no. May, 2011.

[4] J. W. Gauntner, J. N. B. Livingood, and P. Hrycak, "Survey of literature on flow characteristics of a single turbulent jet impinging on a flat plate," *NASA Tech. Memo.*, no. February, p. 43, 1970.

[5] C. Donaldson and R. Snedeker, "A study of free jet impingement. Part 1. Mean properties of free and impinging jets," *J. Fluid Mech*, vol. 45, no. 2, p. 281, 1971.

[6] K. J. Hammad and I. Milanovic, "Flow Structure in the Near-Wall Region of a Submerged Impinging Jet," *J. Fluids Eng.*, vol. 133, no. 9, p. 91205, 2011.

[7] J. Larras, "Plane turbulent impinging jets," *J. Hydraul. Res.*, vol. 12, no. 2, pp. 279–282, 1974.

[8] E. W. Miller, D. R., Comings, "Static pressure distribution in the free turbulent jet," *J. Fluid Mech.*, vol. 3, no. March 1957, pp. 1–16, 1957.

[9] M. N. Wood, "The Static Pressure Distribution Around a Circular Jet Exhausting Normally from a Plane Wall into an Air-stream .," 1965.

[10] S. B. Pope *et al.*, "Turbulent Flows," *J. Turbul.*, vol. 1, no. 0, p. 771, 2000.

[11] B. Scientific, "Some measurements in the self-preservingjet," no. 1969, pp. 1–36, 2005.

[12] D. Cooper, D. C. Jackson, B. E. Launder, and G. X. Liao, "Impinging jet studies for turbulence model assessment-I. Flow-field experiments," *Int. J. Heat Mass Transf.*, vol. 36, no. 10, pp. 2675–2684, 1993.

[13] T. Karimipanah, *Turbulent jets in confined spaces*. 1996.

[14] A. Elsheikh, C. Whitford, R. Hamarashid, W. Kassem, A. Joda, and P. Büchler, "Stress free configuration of the human eye," *Med. Eng. Phys.*, 2013.

[15] A. Elsheikh, "Finite Element Modeling of Corneal Biomechanical Behavior," *J. Refract. Surg.*, vol. 26, no. 4, pp. 289–300, 2010.

[16] A. A. Joda, M. M. S. Shervin, D. Kook, and A. Elsheikh, "Development and validation of a correction equation for Corvis tonometry," *Comput. Methods Biomech. Biomed. Engin.*, vol. 19, no. 9, pp. 943–953, 2015.

[17] A. Eliasy *et al.*, "Ex-vivo experimental validation of biomechanically-corrected intraocular pressure measurements on human eyes using the CorVis ST," *Exp. Eye Res.*, vol. 175, no. June, pp. 98–102, 2018.

[18] M. J. Tummers, J. Jacobse, and S. G. J. Voorbrood, "Turbulent flow in the near field of a round impinging jet," *Int. J. Heat Mass Transf.*, vol. 54, no. 23–24, pp. 4939–4948, 2011.

[19] O. Maklad, V. Theofilis, and A. Elsheikh, "Fluid Structure Interaction (FSI) Simulation of the human eye under the air puff tonometry using Computational Fluid Dynamics (CFD)," in *ICCFD10*, 2018, no. ICCFD10-017.

[20] A. Kotecha, A. Elsheikh, C. R. Roberts, H. Zhu, and D. F. Garway-Heath, "Corneal thickness- and age-related biomechanical properties of the cornea measured with the ocular response analyzer," *Investig. Ophthalmol. Vis. Sci.*, vol. 47, no. 12, pp. 5337–5347, 2006.